Soft Matter

PAPER

View Article Online
View Journal | View Issue

Check for updates

Cite this: *Soft Matter*, 2022, **18**, 1287

Transpiration-powered desalination water bottle

Gracie A. Cornish,†[a] Ndidi L. Eyegheleme,†[b] Laurel S. Hudson,†[c] Kathleen J. Troy,†[d] Maia M. Vollen†[e] and Jonathan B. Boreyko *[b]

Received 12th October 2021,
Accepted 15th December 2021

DOI: 10.1039/d1sm01470f

rsc.li/soft-matter-journal

Inspired by mangrove trees, we present a theoretical design and analysis of a portable desalinating water bottle powered by transpiration. The bottle includes an annular fin for absorbing solar heat, which is used to boost the evaporation rate of water from the interior synthetic leaf. This synthetic leaf comprises a nanoporous film deposited atop a supporting micromesh. Water evaporating from the leaf generates a highly negative Laplace pressure, which pulls the overlying source water across an upstream reverse osmosis membrane. Evaporated water is re-condensed in the bottom of the bottle for collection. The benefit of our hybrid approach to desalination is that reverse osmosis is spontaneously enabled by transpiration, while the thermal evaporation process is enhanced by heat localization and made more durable by pre-filtering the salt. We estimate that a 9.4 cm diameter bottle, with a 10 cm wide annular fin, could harvest about a liter of fresh water per day from ocean water.

Published on 20 January 2022. Downloaded by Virginia Tech on 2/9/2022 2:01:56 PM.

The two central techniques used for water desalination are thermal, where the water is evaporated and re-condensed, and membrane-based, which requires a pressure gradient (reverse osmosis) or electric potential (ion-exchange membrane).[1–4] Both approaches have inherent limitations with regards to efficiency and sustainability. Thermal evaporation suffers from parasitic heat loss into the bulk water.[5–8] This can be remedied by floating heat localizing particles or porous structures at the free surface,[9–26] but these can become compromised over time due to the accumulation of salt crystals.[6,27–29] Membrane-based systems, on the other hand, require considerable positive pressures or large electrical forces, with a power requirement of order $\sim$1 kW h m^{-3}.[30]

The common mangrove tree (*Rhizophora mangle*) can grow in saltwater by employing an ingenious combination of thermal and membrane-based desalination techniques that bypass the inherent constraints of either technique used in isolation.[31–36] Solar thermal evaporation occurs at the water-saturated nanoporous leaf tissue, which produces an absolute negative water pressure that is exploited to achieve reverse osmosis at the salt-excluding roots.[32,34] This negative water pressure is thermodynamically metastable, as described by the cohesion–tension theory, enabling a hydraulic load ($\Delta P \approx$ 30–60 atm) greater than the osmotic pressure of saltwater ($\Delta P \approx$ 25 atm).[32,33] The advantage of this hybrid approach is that the solar evaporation spontaneously drives the reverse osmosis without the active input of pressure or electric potential, such that the entire process is renewable. At the same time, the evaporation process itself benefits from the roots pre-screening the salt, to avoid brine accumulation within the system.[31,34]

Analogous to natural plants, synthetic trees achieve transpiration by exploiting a negative Laplace pressure. The first synthetic tree was developed over 100 years ago, by attaching a glass tube (*i.e.* "xylem" conduit) between two porous ceramics (reservoir and "leaf").[37] More recently, advanced nano/micro-fabrication has enabled sophisticated tree-on-a-chip technology, which has achieved massive suction pressures as high as 100 MPa.[38,39] To date, most synthetic trees only pump water across a single microcapillary tube, which limits their scalability for real-life applications.[37,40–42] However, in 2020 a scalable synthetic tree was demonstrated by connecting 19 plastic tubes in parallel between a water reservoir and a ceramic leaf.[43] In 2021, follow-up works used a solar lamp to boost the evaporation rate of the synthetic leaf and re-condensed the water in a solar still[44] and modeled how the transpiration rate depends on the ambient environment, heat input, and tree geometry.[45]

While most synthetic trees have replenished their water from a freshwater reservoir, Wang *et al.* recently used a saltwater reservoir to demonstrate capillary-driven reverse osmosis at the intake of the system.[32] This mangrove-inspired synthetic tree pumped water upward across a reverse osmosis membrane, to allow for subsequent evaporation from an upper nanoporous membrane. To ensure that water is always in intimate contact with the lower reverse osmosis membrane,

[a] *Cornish School of the Wise, Williamsburg, VA 23188, USA*
[b] *Department of Mechanical Engineering, Virginia Tech, Blacksburg, VA 24061, USA. E-mail: boreyko@vt.edu*
[c] *Cave Spring High School, Roanoke, VA 24018, USA*
[d] *James Madison High School, Vienna, VA 22181, USA*
[e] *George Mason High School, Falls Church, VA 22046, USA*
† Co-first authors and contributed equally.

Published on 20 January 2022. Downloaded by Virginia Tech on 2/9/2022 2:01:56 PM.

the bottom of the synthetic tree was connected to a taller feed reservoir. The throughput of this desalination synthetic tree was minuscule, 1.64 mL h^{-1}, as the transpiration was driven by purely diffusive evaporation into a subsaturated ambient (*i.e.* no heat source).

Here, we theoretically design and model the performance of a renewable, mangrove-inspired desalinating water bottle. Unlike the existing desalinating synthetic tree,[32] we design our bottle with a downward transpiration pathway to avoid the need for a separate feed reservoir. This allows for the bottle to exhibit a compact and portable form factor, where everything is contained within a single columnar structure. By adding an annular solar fin around the bottle that is thermally lumped with the interior nanoporous evaporator, we show that the transpiration rate can be enhanced dramatically. These conceptual innovations will hopefully result in the future real-life engineering of portable water bottles that renewably achieve reverse osmosis.

Conceptual design

The conceptual design of the transpiration-powered desalinating water bottle is shown in Fig. 1. The bottle dimensions were chosen to be 93.8 mm in diameter and approximately 30 cm in height. This is sufficient to hold about 2 L of water, 1 L of saltwater in the top of the bottle and 1 L of purified water in the bottom. The bottle contains six different components to enable desalination. From top to bottom, these components are: (1) input chamber, (2) reverse osmosis membrane, (3) intermediate chamber, (4) synthetic leaf, (5) annular solar disk, and (6) collection chamber.

First, the input chamber is filled with saltwater and then resealed with a twist cap. The bottom of the input chamber is connected to a three-stage reverse osmosis (RO) membrane by means of an O-ring and bolts to maintain an air tight seal. Third, water filtered by the RO membrane flows into a short intermediate chamber, which is similarly attached by another O-ring and bolts. This fresh water then flows into an underlying synthetic leaf that exhibits a planar film of nanopores. Upon evaporating, the water menisci within the nanopores become concave in curvature, which produces a negative Laplace pressure. When the intermediate chamber is full of liquid water, this suction is extended to the overlying RO membrane to enable continuous filtration. The required pre-filling of the intermediate chamber with fresh water could either be facilitated by the manufacturer, or alternately, by the customer prior to bolting on the synthetic leaf. The evaporation rate of water from the synthetic leaf is boosted by designing an annular solar disk that extends beyond the bottle diameter. Finally, water evaporating from the bottom face of the nanoporous film is collected in a bottom compartment, which can hold up to 1 L and can be unscrewed from the bottle for use. Compared to a recent report of transpiration powered desalination,[32] three notable distinctions of our design are the portable bottle design, solar-assisted transpiration rate, and use of a top-down transpiration pathway to avoid the need of a feed reservoir.

This conceptual premise for the desalination water bottle could be realized with practical materials. We envisage the synthetic leaf's nanopores being physically supported within a stainless steel micro-mesh. Using commercially available products as a design guideline, the mesh thickness is t_m = 1 mm

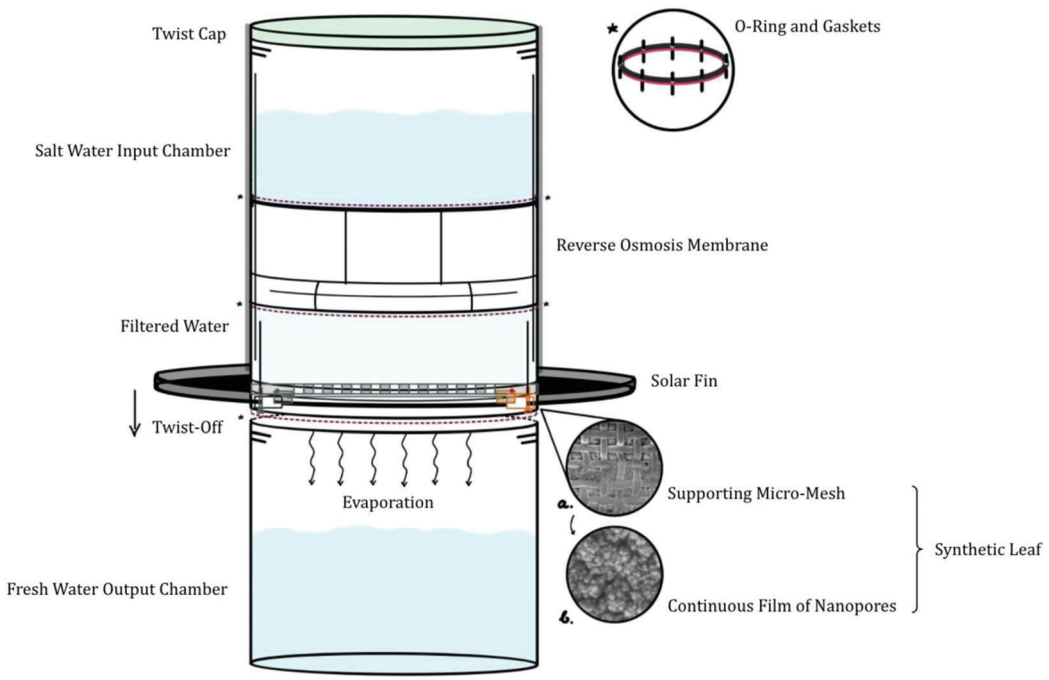

Fig. 1 Conceptual design of the transpiration-powered desalinating water bottle. Not drawn to scale.

 This journal is © The Royal Society of Chemistry 2022

Published on 20 January 2022. Downloaded by Virginia Tech on 2/9/2022 2:01:56 PM.

with micropores of radius $r_{p,m}$ = 0.5 μm. The nanoporous film is deposited on the bottom face of the micro-mesh; an example approach to real-life implementation could be the chemical vapor deposition of nanoporous silicon oxide.[46,47] For the theoretical analysis performed here, the nanopore radius is varied continuously from r_p = 1–100 nm while the thickness of the nanoporous film is either t_n = 10 μm or 100 μm. In other graphs, the nanopore film is now varied continuously from t_n = 1–100 μm while the nanopore radius is either r_p = 5 nm or 50 nm. The solar disk could be comprised of aluminium and spray-coated with a thermally absorptive material, such as graphite. To couple the absorbed heat to the leaf's nanopores, the stainless steel mesh is bolted to the bottom face of the disk where it passes through the interior of the bottle. This interior portion of the aluminum disk includes tunnels to allow for the passage of water into the synthetic leaf. The bottom collector of the bottle should be made from an insulating plastic and is shielded from the sun by the disk, such that it is considerably cooler to promote condensation.

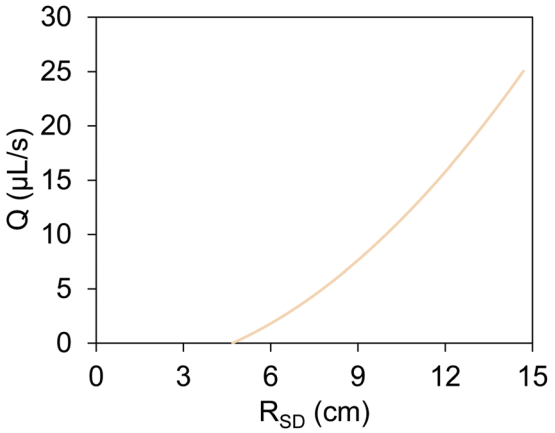

Fig. 2 Transpiration rate *versus* the radius of the solar disk. Values for the transpiration rate are calculated from eqn (1) and (2) for a bottle radius R_B = 4.69 cm, 1 sun of solar irradiation (q_{solar} = 1.0 kW m^{-2}), and the latent heat of vaporization at room temperature (L = 2.43 × 10^6 J kg^{-1}).

Results and discussion

The bottle's transpiration rate can be tuned by the solar disk radius that extends beyond the bottle. Specifically, we estimate the evaporation mass flow rate by relating the amount of irradiation being captured by the disk surface area and crudely assuming a 100% conversion to overcoming the latent heat of vaporization:

$$\dot{m}_v = \frac{\dot{Q}}{L} = \frac{\pi(R_{SD}{}^2 - R_B{}^2)q_{solar}}{L}, \quad (1)$$

where $\dot{Q}$ is the solar power harvested by the disk, L is the latent heat of vaporization, R_B and R_{SD} are the radii of the bottle and the disk, respectively, and q_{solar} is the solar irradiance. Here, we presume daytime conditions corresponding to 1 sun of irradiance: $q_{solar} \approx$ 1.0 kW m^{-2}. The bottle radius is fixed as R_B = 4.69 cm while the radius of the protruding solar disk is varied from $R_{SD} = R_B$ (*i.e.*, no disk) up to R_{SD} = 15 cm.

For any synthetic tree operating at steady-state, the mass flow rate of liquid water is rate-limited by the mass flow rate of evaporation from the leaf.[43] In other words, for mass to be conserved at equilibrium:

$$\dot{m}_v = \dot{m} = \rho Q. \quad (2)$$

where m_v is the leaf's evaporative mass flow rate and $\dot{m}$, ρ, and Q are the liquid's mass flow rate, density, and volumetric flow rate across the tree, respectively. Mass conservation is a reasonable assumption because $\dot{m}_v < \dot{m}$ would mandate the compressibility of incompressible water, while $\dot{m}_v > \dot{m}$ would keep decreasing the menisci's contact angle until achieving a Laplace pressure where $\dot{m}_v = \dot{m}$ is satisfied (or dryout occurs).

Fig. 2 uses eqn (1) and (2) to solve for the mass flow rate of liquid water into the bottle's collector. As expected, the transpiration rate increases non-linearly with increasing disk radius, as the larger surface area will capture more solar irradiation. For the largest disk considered, R_{SD} = 14.69 cm (*i.e.*, annular width of 10 cm), the transpiration rate is $Q \approx$ 25 μL s^{-1}, which over the span of 12 h results in 1.08 L of collected water. These calculations assumed that all of the evaporated water could condense into liquid water in the collector; this assumption may break down at sufficiently high transpiration rates where the cooling rate of the collector becomes rate-limiting.

In Fig. 3, the various pressure drops across the water bottle are graphed as functions of the effective radius of the leaf's nanopores. The bottle's transpiration rate was defined by the radius of the solar disk, either R_{SD} = 14.69 cm with $Q \approx$ 25 μL s^{-1} (Fig. 3a and b) or R_{SD} = 10.89 cm with $Q \approx$ 12.5 μL s^{-1} (Fig. 3c and d). The pressure drop across the reverse osmosis membrane is given by:[32]

$$\Delta P_{RO} = \left(\frac{Q}{A_B \kappa_w} + \Pi\right), \quad (3)$$

where Π is the osmotic pressure (25 bar for seawater), A_B is the cross-sectional area of the water bottle, and $\kappa_w = (\Phi r_p{}^2 l_{RO})/(8\mu\tau)$ is the water permeability coefficient of the RO membrane, where Φ is the membrane porosity, μ is the liquid water viscosity, l_{RO} is the length of the membrane ($\approx$200 nm), and τ is the tortuosity. A permeability of $\kappa_w \approx 2.7 \times 10^{-7}$ m s^{-1} bar^{-1} was reported by Elimilech *et al.*, for experiments carried out on commercially available RO membranes.[32] Here, we vary the osmotic pressure of the feedwater as either 25 bar (for regular seawater), 100 bar, or 250 bar. The higher values of Π account for when the solute concentration increases as the water passes through the RO membrane over time.

Darcy's Law is used to estimate the viscous pressure drops across the microporous mesh and nanoporous membrane:

$$\Delta P_D = \frac{Qt}{\kappa A_B}, \quad (4)$$

where t is the thickness of either the micro-mesh (t_m) or nanopores (t_n) and κ is the intrinsic permeability of the mesh (κ_m) or the nanopores (κ_n). The mesh thickness was fixed at

Published on 20 January 2022. Downloaded by Virginia Tech on 2/9/2022 2:01:56 PM.

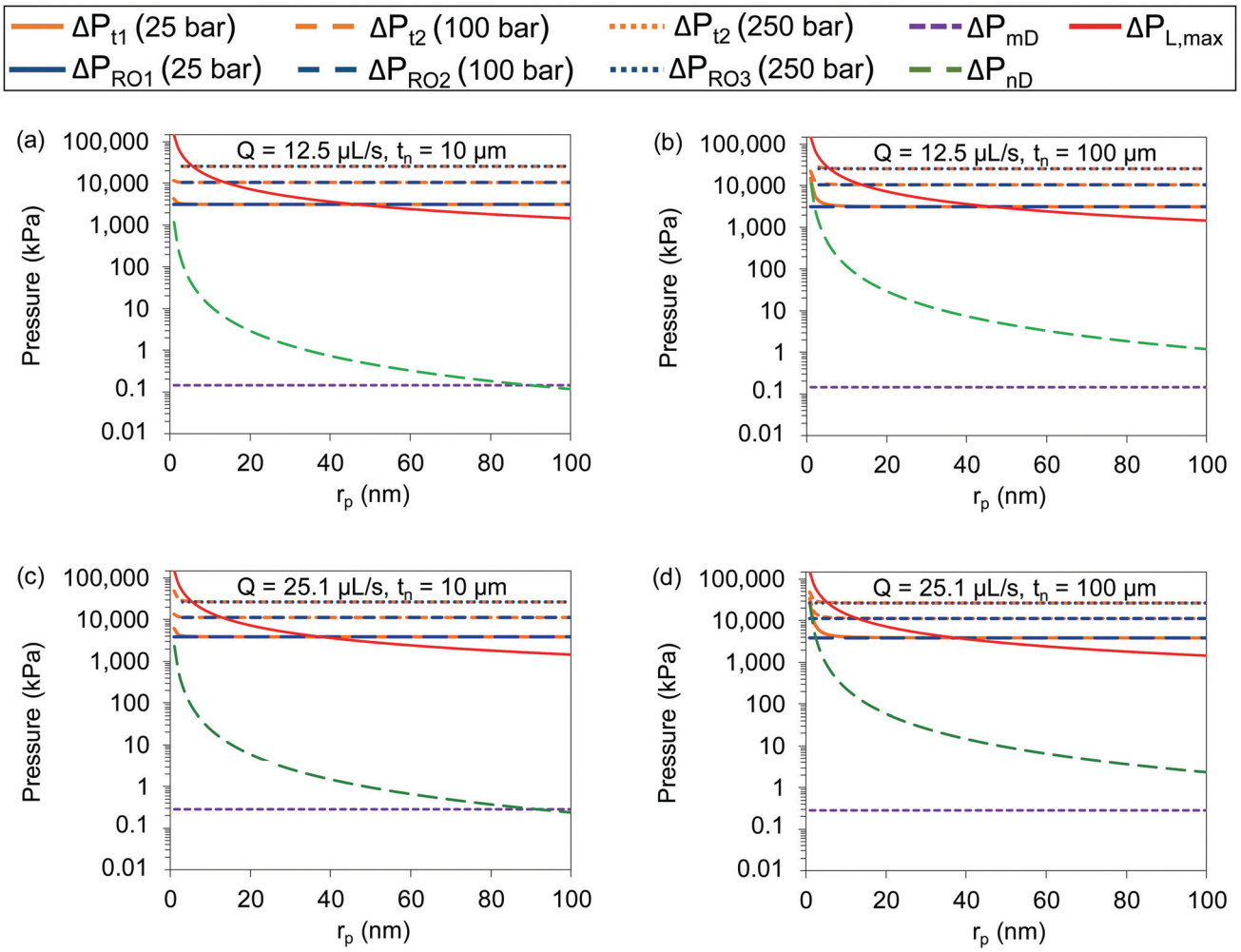

Fig. 3 Pressure drops *versus* the leaf's nanopore radius. The various pressure drops were calculated from eqn (3)–(5) and (7). The multiple curves for the reverse osmosis pressure drop (blue) and, by extension, the total pressure drop (orange) account for the increasing solute concentration of the feedwater over the course of the day. The bottle radius and micropore thickness were fixed at R_B = 4.69 cm, and t = 1 mm, respectively, while the volumetric flow rate and nanopore thickness were varied as (a) $Q \approx 12.5$ μL s^{-1} corresponding to R_{SD} = 10.89 cm and t = 10 μm, (b) $Q \approx 12.5$ μL s^{-1} and t = 100 μm, (c) $Q \approx 25$ μL s^{-1} corresponding to R_{SD} = 14.69 cm and t = 10 μm, and (d) $Q \approx 25$ μL s^{-1} and t = 100 μm.

t_m = 1 mm, while t_n varied. In turn, $\kappa = (\varphi r_p^2)/(8\mu\tau)$, where μ is the water's viscosity, $r_{p,m} \approx 500$ nm is the fixed pore radius of the mesh, $\varphi_m \approx 0.36$ is the mesh porosity, $\tau_m \approx 1$ is the mesh tortuosity, and the nanopores exhibit $\varphi_n \approx 0.33$ and $\tau_n \approx 3$ while $r_{p,n}$ was varied. The Poiseuille equation is used to estimate the viscous pressure drop in the intermediate space between the RO filter and the synthetic leaf: $\Delta P_P = (8QH\mu)/(\pi R_B^4)$, where H = 1 cm is the height of this space and the other variables are the same as defined earlier.

The total pressure drop across the water bottle is then:

$$\Delta P_t = \Delta P_{RO} + \Delta P_{mD} + \Delta P_{nD} + \Delta P_P, \quad (5)$$

where P_{mD} and ΔP_{nD} are the Darcy pressure drops across the microporous mesh and nanoporous membrane, respectively. The hydrostatic pressure of the intermediate liquid column within the bottle (H = 1 cm) is negligible. The three estimates of RO membrane pressure drops are represented by ΔP_{RO1} corresponding to an osmotic pressure of Π_1 = 25 bar, ΔP_{RO2} for Π_1 = 100 bar, or ΔP_{RO3} for Π_1 = 250 bar. This results in three different calculations of the total pressure drop across the bottle: ΔP_{t1} (for 25 bar), ΔP_{t2} (100 bar), and ΔP_{t3} (250 bar). Combining eqn (1) and (2) to solve for Q, we can then solve eqn (5) for ΔP_t for any given bottle geometry. This positive pressure drop across the bottle is facilitated by a negative Laplace pressure of equivalent magnitude, generated from concave menisci within the leaf's nanopores:

$$\Delta P_t = |P_L| = \frac{2\gamma \cos\theta}{r_p}, \quad (6)$$

where γ is the surface tension of the air–water interface and θ is the contact angle each meniscus makes with the side walls of its pore. For any given pressure drop across the bottle, there is only one value of θ that will satisfy eqn (6). The maximum

 This journal is © The Royal Society of Chemistry 2022

Published on 20 January 2022. Downloaded by Virginia Tech on 2/9/2022 2:01:56 PM.

possible Laplace suction corresponds to when the menisci reach their receding contact angle, $\theta = \theta_R$:

$$|P_{L,max}| = \frac{2\gamma \cos \theta_R}{r_p}. \quad (7)$$

Fig. 3 graphs the dependence of the various pressure drops on the leaf's nanopore radius, for two different transpiration rates and two different choices of t_n. ΔP_{RO} is independent of the synthetic leaf's properties and is the dominant pressure drop for the vast majority of the parameter space, such that $P_t \approx \Delta P_{RO}$. The exception to this is when the Darcy pressure drop across the leaf becomes appreciable at sufficiently small nanopore radii in the leaf. The nano-Darcy pressure increases non-linearly with decreasing r_p, due to the associated decrease in permeability. As a consequence, P_{nD} contributes appreciably to P_t for $r_p < 10$ nm when $t_n = 100$ μm and for $r_p < 2$ nm when $t_n = 10$ μm. When $t_n = 100$ μm, the nano-Darcy pressure actually exceeds even the reverse osmosis pressure beneath a critical pore size of $r_p \approx 2$ nm. The micro-Darcy pressure drop is four orders of magnitude smaller than ΔP_{RO1} and therefore has no appreciable effect on ΔP_t. Likewise, the Poiseuille pressure drop has no contribution to ΔP_t, as it is about 14–15 orders of magnitude smaller than ΔP_{RO1}. The maximum Laplace suction, $|P_{L,max}|$, decreases linearly with increasing r_p.

Transpiration-powered desalination breaks down beyond a critical r_p where $|P_{L,max}| > P_t$ for the first time. In other words, the bottle is no longer operational when a given orange curve (P_t) falls beneath the red curve ($|P_{L,max}|$). For the bottle geometries considered here, breakdown occurred at $r_p \approx 46.0$ nm for Fig. 3(a and b), and $r_p \approx 37.5$ nm for Fig. 3(c and d) for seawater ($\Pi = 25$ bar, P_{t1}), at $r_p \approx 13.5$ nm for Fig. 3(a and b), and $r_p \approx 12.5$ nm for Fig. 3(c and d) for $\Pi = 100$ bar (P_{t2}), and at $r_p \approx 5.5$ nm for Fig. 3(a–d), for $\Pi = 250$ bar (P_{t3}). These critical values were independent of the bottle transpiration rate, as breakdown occurred where the Darcy pressures were negligible compared to P_{RO1}.

Fig. 4 illustrates how varying the nanopore thickness affects the various pressure drops. As the nanopore thickness increases, the nano-Darcy pressure increases linearly (eqn (4)). When comparing transpiration rates of $Q = 12.5$ μL s^{-1} (Fig. 4a) and $Q = 25$ μL s^{-1} (Fig. 4b) for $r_{np} = 5$ nm, the curves for the nano-Darcy and micro-Darcy pressures both shift up by roughly a factor of two. The other pressure drops: ΔP_{RO}, ΔP_P, ΔP_{mD}, and $P_{L,max}$ are all independent of the nanopore thickness. The pressure drop to achieve reverse osmosis is the dominant pressure drop by 1–4 orders of magnitude, such that $\Delta P_t \approx \Delta P_{RO}$ is generally true until a thickness is reached in which ΔP_{nD} out-competes ΔP_{RO}. For the

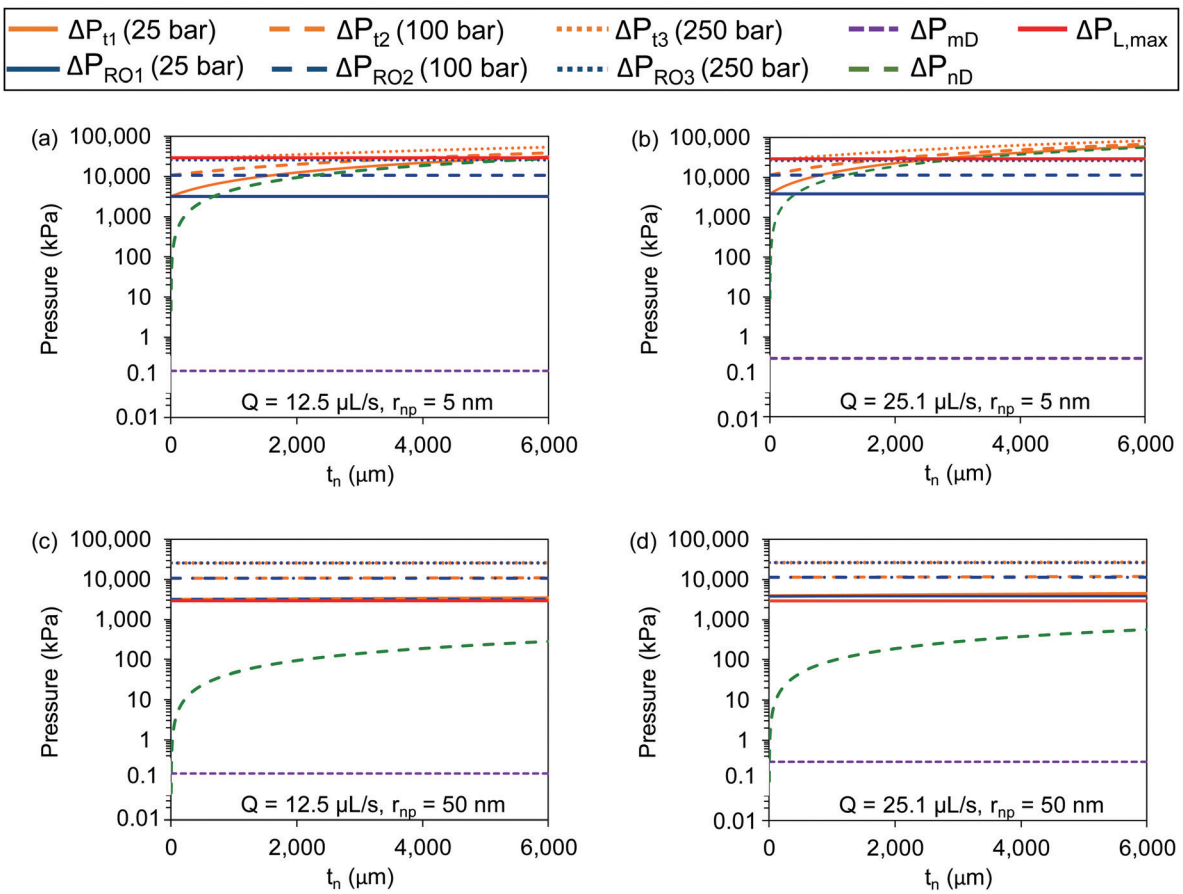

Fig. 4 Pressure drops *versus* the leaf's nanopore thickness. The various pressure drops were calculated in the same manner as Fig. 3, but here the nanopore radius was varied as (a and b) $r_p = 5$ nm or (c and d) $r_p = 50$ nm.

Published on 20 January 2022. Downloaded by Virginia Tech on 2/9/2022 2:01:56 PM.

smaller transpiration rate of $Q = 12.5\ \mu L\ s^{-1}$ (Fig. 4a) this occurs at $t_n = 678\ \mu m$ for $\Pi = 25$ bar, at $t_n = 2281\ \mu m$ for $\Pi = 100$ bar and at $t_n = 5486\ \mu m$ for $\Pi = 250$ bar. For the larger transpiration rate of $Q = 25\ \mu L\ s^{-1}$ (Fig. 4b), ΔP_{nD} surpasses ΔP_{RO} at $t_n = 411\ \mu m$ for $\Pi = 25$ bar, at $t_n = 1209\ \mu m$ for $\Pi = 100$ bar and at $t_n = 2807\ \mu m$ for $\Pi = 250$ bar. For nanopore thicknesses above these values, the nano-Darcy pressure drop becomes dominant and strongly increases the total pressure drop. As with Fig. 3, the Poiseuille pressure drop was not graphed, as ΔP_P is about 14–15 orders of magnitude smaller than ΔP_{RO}. For $r_p = 5$ nm, the total pressure drop was an order of magnitude smaller than $|P_{L,max}| = 29.2$ MPa (assuming $\theta_R = 0^\circ$) for small values of t_n. Bottle operation broke down ($|P_{L,max}| > P_t$) above a critical nanopore thickness of $t_n = 5563\ \mu m$, $t_n = 3960\ \mu m$, and $t_n = 754\ \mu m$ for $\Pi = 25$ bar, 100 bar, and 250 bar, respectively for $Q = 12.5\ \mu L\ s^{-1}$. For the higher flow rate of $Q = 25\ \mu L\ s^{-1}$, breakdown occurs beyond $t_n = 2710\ \mu m$, $t_n = 1902\ \mu m$, and $t_n = 304\ \mu m$, respectively.

Fig. 4c and d increases the nanopore size to $r_{np} = 50$ nm, again varying t_n for two different transpiration rates. This increase in permeability serves to decrease ΔP_{nD} by two orders of magnitude, such that ΔP_{mD} actually exceeds ΔP_{nD} for $t_n < 4\ \mu m$. This reduction in ΔP_{nD} also means that P_{RO} completely dominates the pressure drops, even for the largest nanopore thicknesses. Across the entire parameter space, $P_t \approx P_{RO}$ is slightly larger than $|P_{L,max}|$, which reveals the fatal design flaw of using $r_{np} = 50$ nm for desalination. In other words, even the maximum possible Laplace suction is insufficient for overcoming the reverse osmosis pressure, even when all other pressure drops are negligible. This clearly indicates the importance of using sufficiently small nanopores, *i.e.*, $r_{np} < 50$ nm, when using transpiration to desalinate ocean water.

Beyond a critical water salinity, the bottle can no longer filter water. For example, consider a bottle where $t_n = 0.1$ mm, $r_{p,n} = 5$ nm, and $Q = 25\ \mu L\ s^{-1}$. A breakdown in the system performance will occur when $\Delta P_t \geq |P_{L,max}| = 29.2$ MPa. With all other pressure drops remaining constant at the given flow rate, we can back out the value of ΔP_{RO} where $\Delta P_t = |P_{L,max}|$ from eqn (5), and then solve for the critical osmotic pressure (Π) of the feedwater from eqn (3). This yields $\Pi = 269.16$ bar, which corresponds to a critical molarity of $5.43\ mol\ L^{-1}$ from $\Pi = MRTi$, where M is the number of moles per liter of solution, R is the universal gas constant, T is the temperature, and i is the van't Hoff factor (2 for NaCl). For a constant number of moles of solute, $n_s = M_i V_i = M_f V_f$, where V_i and M_i are the initial volume and molarity of feedwater put into the input chamber, while V_f and M_f are the final volume and molarity of feedwater remaining in the input chamber after a day's operation. For a daily collection goal of $V_w = 1.08$ L desalinated in the bottle's collector, the minimum amount of seawater ($M_i \approx 0.5\ mol\ L^{-1}$) that must be fed into the bottle is $V_i \geq V_w + V_{f,c}$, such that the molarity of the feedwater doesn't exceed the critical value of $M_{f,c} \approx 5.43\ mol\ L^{-1}$ by the end of the day. Simultaneously solving $M_i V_i = M_{f,c} V_{f,c}$ and $V_i = V_w + V_{f,c}$ yields $V_i = V_w/(1 - M_i/M_{f,c}) = 1.19\ L$ of seawater, *i.e.*, the volume of seawater input into the bottle must be at least 110% of the desired fresh water output for this particular bottle design.

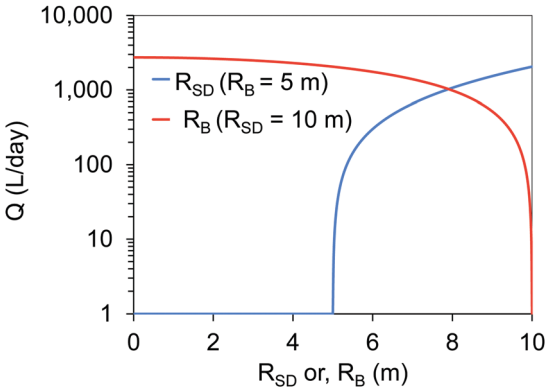

Fig. 5 Semi-log plot of the daily volume of harvested water *versus* the disk radius (blue line) or water bottle radius (red). Curves are generated using eqn (1) for a fixed bottle radius of $R_B = 5$ m or a fixed solar disk radius of $R_{SD} = 10$ m.

The above results were for a portable-sized water bottle, where the bottle and solar disk radii were 4.69 cm and up to 15 cm, respectively. This resulted in a transpiration rate of up to $Q \approx 25\ \mu L\ s^{-1}$, which corresponds to about 1.08 L per day. If we consider a worst-case scenario, with a reduced solar illumination of $700\ W\ m^{-2}$ and only a 70% solar-thermal conversion efficiency, the volume collected would be only 0.53 L per day. However, if freed from the constraint of a portable bottle, the same concept could be applied to larger systems to harvest much greater amounts of water. Fig. 5 depicts how the daily volume of harvested water changes with a widely varying disk radius (for a fixed $R_B = 5$ m) or varying bottle radius (for a fixed $R_{SD} = 10$ m). In either of the two scenarios, $\dot{m}$ was calculated from eqn (1) and (2) and the daily amount was then calculated assuming 12 hours of sunshine. Over the valid parameter space of $R_{SD} > R_B$, transpiration rates as large as $Q \sim 1000\ L\ day^{-1}$ are possible when the solar disk radius is at least 3 m larger than the bottle radius. For such large volumes of harvested water, there is the caveat that active cooling at the condenser is almost certainly necessary. Otherwise, the condensation rate would be rate-limiting, as opposed to the transpiration rate.

To summarize, we conceptually designed and theoretically analyzed a transpiration-powered desalinating water bottle. From top to bottom, the bottle design is comprised of an input chamber connected to a reverse osmosis membrane, an intermediate chamber connected to a synthetic leaf, and an output chamber that condenses vapor emanating from the leaf. The synthetic leaf is comprised of a nanoporous membrane suspended across the bottom face of a microporous mesh. The negative Laplace pressure generated by the concave menisci within the nanopores is what provides the suction necessary to overcome reverse osmosis at the intake filter. The transpiration rate is boosted by adding an annular solar disk around the bottle. Our analytical model found that reverse osmosis can be achieved when the leaf's nanopores satisfy $r_p < 50$ nm and the transpiration rate is approximately $1\ L\ day^{-1}$ when using a bottle radius of $R_B = 4.69$ cm and a disk radius of $R_{SD} = 15$ cm. We hope that our mangrove-inspired design will lead to the development of renewable and portable desalination technology.

 This journal is © The Royal Society of Chemistry 2022

Published on 20 January 2022. Downloaded by Virginia Tech on 2/9/2022 2:01:56 PM.

Conflicts of interest

The authors declare that they have no competing interests.

Acknowledgements

This work was supported by a National Science Foundation CAREER Award (CBET-1653631). We are grateful to the Center for the Enhancement in Engineering Diversity (CEED), which facilitated the C-Tech^2 summer camp where the high-school students conceived the idea and met Prof. Boreyko. The fabrication and SEM imaging of the proposed synthetic leaf materials were conducted at the Center for Nanophase Materials Sciences (User Project #CNMS2021-R-00748), which is a DOE Office of Science User Facility. We thank Patrick Collier, Dale Hensley, Nickolay Lavrik, and Bernadeta Srijanto for technical assistance.

Notes and references

1 M. Abbas, H. Aburideh, Z. Tigrine, N. K. Merzouk and A. Hamadene, 2017 International Renewable and Sustainable Energy Conference (IRSEC), 2017, pp. 1-4.
2 P. G. Youssef, R. K. Al-Dadah and S. M. Mahmoud, *Energy Precedia*, 2014, **61**, 2604–2607.
3 K. G. Nayar, P. Sundararaman, C. L. O'Connor, J. D. Schacherl, M. L. Heath, M. O. Gabriel, S. R. Shah, N. C. Wright and A. V. Winter, *Dev. Eng.*, 2017, **2**, 38–46.
4 T. Qui and P. A. Davies, *Water*, 2012, **4**, 690–706.
5 Z. Yu, C. Li, L. Li, J. Yang and S. Cheng, *ACS Appl. Mater. Interfaces*, 2019, **11**, 32038–32045.
6 Z. Liu, B. Wu, B. Zhu, Z. Chen, M. Zhu and X. Liu, *Adv. Funct. Mater.*, 2019, **29**, 1905485.
7 Z. Li, C. Wang, T. Lei, H. Ma, J. Su, S. Ling and W. Wang, *Adv. Sustainable Syst.*, 2019, **3**, 1800144.
8 N. Xu, X. Hu, W. Xu, X. Li, L. Zhou, S. Zhu and J. Zhu, *Adv. Mater.*, 2017, **29**, 1606762.
9 H. Ghasemi, G. Ni, A. M. Marconnet, J. Loomis, S. Yerci, N. Miljkovic and G. Chen, *Nat. Commun.*, 2014, **5**, 4449.
10 L. Zhang, B. Tang, J. Wu, R. Li and P. Wang, *Adv. Mater.*, 2015, **27**, 4889–4894.
11 C. Chang, C. Yang, Y. Liu, P. Tao, C. Song, W. Shang, J. Wu and T. Deng, *ACS Appl. Mater. Interfaces*, 2016, **8**, 23412–23418.
12 Y. Ito, Y. Tanabe, J. Han, T. Fujita, K. Tanigaki and M. Chen, *Adv. Mater.*, 2015, **27**, 4302–4307.
13 Y. Liu, S. Yu, R. Feng, A. Bernard, Y. Liu, Y. Zhang, H. Duan, W. Shang, P. Tao, C. Song and T. Deng, *Adv. Mater.*, 2015, **27**, 2768–2774.
14 Y. Liu, J. Chen, D. Guo, M. Cao and L. Jiang, *ACS Appl. Mater. Interfaces*, 2015, **7**, 13645–13652.
15 J. Lou, Y. Liu, Z. Wang, D. Zhao, C. Song, J. Wu, N. Dasgupta, W. Zhang, D. Zhang, P. Tao, W. Shang and T. Deng, *ACS Appl. Mater. Interfaces*, 2016, **8**, 14628–14636.
16 Q. Jiang, L. Tian, K. K. Liu, S. Tadepalli, R. Raliya, P. Biswas, R. R. Naik and S. Singamaneni, *Adv. Mater.*, 2016, **28**, 9400–9407.
17 C. Liu, J. Hsiung, Y. Tian, J. Wang, Y. Han and A. Fratalocchi, *Adv. Sustainable Syst.*, 2017, **1**, 1600013.
18 H. Zhang, L. Li, B. Jiang, Q. Zhang, J. Ma, D. Tang and Y. Song, *ACS Appl. Mater. Interfaces*, 2020, **12**, 16503–16511.
19 K. Bae, G. Kang, S. K. Cho, W. Park, K. Kim and W. J. Padilla, *Nat. Commun.*, 2015, **6**, 10103.
20 M. Jiang, Q. Shen, J. Zhang, S. An, S. Ma, P. Tao, C. Song, B. Fu, J. Wang, T. Deng and W. Shang, *Adv. Funct. Mater.*, 2020, **30**, 1910481.
21 L. Zhou, Y. Tan, D. Ji, B. Zhu, P. Zhang, J. Xu, Q. Gan, Z. Yu and J. Zhu, *Sci. Adv.*, 2016, **2**, e1501227.
22 S. Han, J. Yang, X. Li, W. Li, X. Zhang, N. Koratka and Z. Yu, *ACS Appl. Mater. Interfaces*, 2020, **12**, 13229–13238.
23 K. Liu, Q. Jiang, S. Tadepalli, R. Raliya, P. Biswas, R. R. Naik and S. Singamaneni, *ACS Appl. Mater. Interfaces*, 2017, **9**, 7675–7681.
24 F. Liu, L. Wang, R. Bradley, B. Zhao and W. Wu, *Adv. Sustainable Syst.*, 2020, **4**, 1900122.
25 C. Tian, J. Liu, R. Ruan, X. Tian, X. Lai, L. Xing, Y. Su, W. Huang, Y. Cao and J. Tu, *Small*, 2020, **16**, 2000573.
26 K. Go, K. Bae, H. Choi, H. Y. Kim and K. J. Lee, *ACS Appl. Mater. Interfaces*, 2019, **11**, 48300–48308.
27 A. M. K. El-Ghonemy, *Alex. Eng. J.*, 2018, **57**, 2401–2413.
28 L. Wu, Z. Dong, Z. Cai, T. Ganapathy, N. X. Fang, C. Li, C. Yu, Y. Zhang and Y. Song, *Nat. Commun.*, 2020, **521**, 11.
29 M. Zhu, Y. Li, G. Chen, F. Jiang, Z. Yang, X. Luo, Y. Wang, S. D. Lacey, J. Dai, C. Wang, C. Jia, J. Wan, Y. Yao, A. Gong, B. Yang, Z. Yu, S. Das and L. Hu, *Adv. Mater.*, 2017, **29**, 1704107.
30 M. Elimelech and W. A. Phillip, *Science*, 2011, **333**, 712–717.
31 R. Reef and C. E. Lovelock, *Ann. Bot.*, 2015, **115**, 385–395.
32 Y. Wang, J. Lee, J. Weber and M. Elimelech, *Sci. Adv.*, 2020, **6**, eaax5253.
33 P. F. Scholander, *Physiol. Plant.*, 1968, **21**, 251–261.
34 K. Kim, E. Seo, S. K. Chang, T. J. Park and S. J. Lee, *Sci. Rep.*, 2016, **6**, 20426.
35 A. D. Stroock, V. V. Pagay, M. A. Zwieniecki and N. M. Holbrook, *Annu. Rev. Fluid Mech.*, 2014, **46**, 615–642.
36 A. K. Parida and B. Jha, *Trees*, 2010, **24**, 199–217.
37 H. H. Dixon and J. Joly, *Philos. Trans. R. Soc., B*, 1895, **186**, 563–576.
38 T. D. Wheeler and A. D. Stroock, *Nature*, 2008, **455**, 208–212.
39 O. Vincent, A. Szenicer and A. D. Stroock, *Soft Matter*, 2016, **12**, 6656–6661.
40 H. Thut, *Ohio J. Sci.*, 1928, **28**, 292–298.
41 A. T. J. Hayward, *Nature*, 1970, **225**, 376–377.
42 M. Lee, H. Lim and J. Lee, *Sci. Rep.*, 2017, **7**, 14735.
43 W. Shi, R. Dalrymple, C. McKenny, D. Morrow, Z. Rashed, D. Surinach and J. Boreyko, *Sci. Rep.*, 2020, **10**, 230.
44 N. L. Eyegheleme, W. Shi, L. H. D. Koninck, J. L. O'Brien and J. B. Boreyko, *Appl. Phys. Lett.*, 2021, **118**, 251601.
45 N. L. Eyegheleme, K. Peng and J. B. Boreyko, *Int. J. Heat Mass Transfer*, 2022, **183**, 122121.
46 J. J. Charlton, N. Lavrik, J. A. Bradshaw and M. J. Sepaniak, *ACS Appl. Mater. Interfaces*, 2014, **6**, 17894–17901.
47 D. R. Lincoln, N. V. Lavrik, I. I. Karvchenko and M. J. Sepaniak, *Anal. Chem.*, 2016, **88**, 8741–8748.